Trans Indian Inst Met (2024) 77(2):583–591
https://doi.org/10.1007/s12666-023-03130-w

ORIGINAL ARTICLE

Study of Microstructure and Mechanical Properties of Short Carbon Fibers Reinforced Mg Matrix Composites Fabricated by Hot Extrusion

Zhao Yang[1,2,3,4] · Hong-yu Xu[1] · Bo Jiang[1] · Ye Wang[1] · Mao-liang Hu[1] · Ze-sheng Ji[1]

Received: 17 June 2023 / Accepted: 25 September 2023 / Published online: 3 November 2023

Abstract This study investigated the effect of extrusion ratio on the microstructural evolution and mechanical properties of the as-extruded short carbon fibers (SCFs) reinforced AZ31 alloy composite, and the microstructural development of the composite during extrusion was thoroughly investigated. The dominant dynamic recrystallization (DRX) mechanisms are particle simulated nucleation, continuous DRX, and discontinuous DRX. The addition of SCFs promotes the dynamic recrystallization during hot extrusion. As extrusion ratio increases, the interfacial bonding degree of the composite increases gradually, and the composite with an extrusion ratio of 25:1 exhibits the finest DRXed grains and the best mechanical performance with a yield strength of 171 MPa, an ultimate tensile strength of 258 MPa and an elongation of 6.0%. The enhanced strength is mainly attributed to grain refinement strengthening and dislocation strengthening, which are induced by the DRXed grains and the added SCFs.

✉ Zhao Yang
zhaoyang@ahpu.edu.cn

✉ Hong-yu Xu
xuhongyu@hrbust.edu.cn

1 School of Material Science and Chemical Engineering, Harbin University of Science and Technology, Harbin 150080, People's Republic of China

2 School of Materials Science and Engineering, Anhui Polytechnic University, Wuhu 241000, People's Republic of China

3 Anhui Key Lab High Performance Nonferrous Met Mat, Anhui Polytech Univ, Wuhu 241000, People's Republic of China

4 Key Laboratory of Additive Manufacturing (3D Printing) of Anhui Province, Wuhu 241000, People's Republic of China

Keywords Magnesium matrix composite · Extrusion ratio · Microstructure · Dynamic recrystallization · Mechanical properties

1 Introduction

Magnesium matrix composites are well-known for their light weight, high specific strength and high specific modulus, which make them receive increasing interest in the field of aerospace and automobile [1–3]. Typically, discontinuously reinforced magnesium matrix composites as isotropic materials exhibit excellent mechanical properties and easy processability [4]. For instance, Nie et al. [5] prepared TiCnp/Mg–Zn-Sr-Ca composites with a yield strength of over 500 MPa after multidirectional forging and extrusion. The recrystallization volume fraction of the composites (99%) was noticeably higher than that of the alloys (58%), which improved the yield strength greatly. Wang et al. [6] developed a bimodal size SiC particle-reinforced magnesium matrix composites with high strength, which are enhanced by grain refinement and load transfer. Xiong et al. [7] fabricated short carbon fibers reinforced Nb/Nb_5Si_3 composites by ball milling and spark plasma sintering. They found that the interface debonding and fiber pull-out behavior are the dominant toughening mechanisms of the short carbon fiber reinforced Nb/Nb_5Si_3 composites. Further, the addition of short carbon fibers with large size can stimulate the nucleation of dynamic recrystallization [8, 9]. Therefore, previous studies have shown that grain refinement can be used as an effective way to enhance the performance of the composites. However, the effect of discontinuous reinforcement on the dynamic recrystallization behavior of magnesium matrix composites has been rarely studied.

As is well-known, hot extrusion is an effective process to fabricate magnesium matrix composites, which can be beneficial for optimizing microstructure and improving mechanical strength and ductility [10–12]. Yuan et al. [13] applied hot extrusion to synthesize graphene/AZ91 composite by sinter, the as-extruded composite can achieve the yield strength and elongation of 296 MPa and 8.7%, respectively. Nie et al. [14] developed TiCp/Mg-Zn-Ca composite by using an ultrasonic-assisted semisolid stirring and extrusion process. The results showed that the formability at the lower extrusion temperature of the composite is improved, which contributed to TiCp addition and high DRXed fraction. Hence, it is essential to select an appropriate extrusion condition, including extrusion temperature, extrusion speed, and extrusion ratio [15]. With different extrusion conditions, the composite has different morphologies and distribution of reinforcement [16]. Among them, a proper extrusion ratio could effectively realize uniform and dispersed distribution of discontinuous reinforcement by large accumulated strain and abundant material flow [17, 18]. However, less attention has been paid to understanding the effect of extrusion ratio on the microstructure and properties of discontinuously reinforced magnesium composites fabricated by solid-state synthesis process.

In this study, AZ31 alloy was selected as a matrix, while short carbon fibers (SCFs) were used as reinforcement particles. The SCFs reinforced AZ31 composite was fabricated by a solid-state synthesis process, including hot-press and hot extrusion. The effect of different extrusion ratios on the microstructure and mechanical properties of the SCFs/AZ31 composite were studied, and the effect of discontinuous reinforcement on dynamic recrystallization behavior of composites was analyzed in detail.

2 Experimental Procedures

The reinforcement was short carbon fibers with a cross-sectional diameter of 7–8 μm, which is virgin and provided by Xiang Sheng Carbon Fiber Company (Yan cheng, China). The matrix in the paper was Mg-2.8Al-1.0Zn-0.25Mn (wt.%) (AZ31) alloy. AZ31 alloy chips were mechanically cut from AZ31 alloy ingot, and the size of chips was about 4 mm × 2 mm × 0.3 mm.

The SCFs/AZ31 composite was fabricated by the solid-state synthesis. Firstly, the SCFs and AZ31 chips were ball-milled at 400 rpm for 30 min, using stainless steel balls with a ball-to-mixtures weight ratio of 8:1. Secondly, the mixtures of SCFs and AZ31 chips were hot-pressed to a cylindrical billet with a diameter of 40 mm at 350 °C. Finally, the billet was preheated at 400 °C for 30 min, followed by direct extrusion with a ram speed of 0.8 mm/s and extrusion ratios of 8:1, 11:1, 25:1, and 44:1, which were denoted at R8, R11, R25, and R44, respectively.

The microstructures of the SCFs/AZ31 composite were studied with an OLYMPUS-GX71-6230A optical microscopy (OM), Quanta-200 scanning electron microscope (SEM) with energy-dispersive X-ray spectroscopy (EDS), and TESCAN MAIA3 scanning electron microscope (SEM) with Nordlys Max3 electron backscattered diffraction (EBSD) apparatus, and the data were analyzed by HKL-Channel 5 Analysis software.

Dog-bone-shaped tensile specimens having gauge length and width of 35 mm and 8 mm were used based on the ASTM E8/E8M-16a. The tensile test with a speed of 1 mm/min was conducted on an Instron 5500R universal testing machine at room temperature, the loading direction was along the extrusion direction (ED), and four repeated tests for each sample were performed.

3 Results and Discussion

3.1 Microstructure of the Hot-Pressed Samples

The morphology of the hot-pressed SCFs/AZ31 billets revealed that the bond interface of chips displayed a network-like pattern with some wide regions (Fig. 1a), and some gray particles distributed in the Mg matrix (Fig. 1b). Combining with the results of EDS elemental maps of C, O, Mg, Al, Zn, and Mn obtained from the hot-pressed billets, the secondary phase particles in the bond interface of chips are SCFs and the particles distributed in the matrix are enriched by Al and Mn, and they may be Al_8Mn_5 phases [19]. Zn elements dissolve in the Mg matrix. Furthermore, the EDS elemental maps show that the O element exists at the same position as the C element, distributing along the interface of AZ31 chips. Mg alloys are easy to be oxidated; during the process of turning Mg chips, the oxide layers are formed in exposed surfaces, which introduces the O element in hot-pressed billets.

3.2 Microstructure of the As-Extruded Samples

Figure 2 shows the low-magnification OM images of the as-extruded R8, R11, R25, and R44 composites. The microstructures of the composites clearly indicate that full dynamic recrystallization (DRX) occurs in all extruded composites. After hot extrusion, the SCFs bands exhibit varying degrees of elongation in the longitudinal section. The SCFs band is not aligned along the extrusion direction in the R8 sample, as shown in Fig. 2a. While increasing the extrusion ratio, the direction of the SCFs band tends to parallel the extrusion direction (Fig. 2b–d), which indicates that the larger extrusion ratio lead to the increase in deforming degree of the matrix as

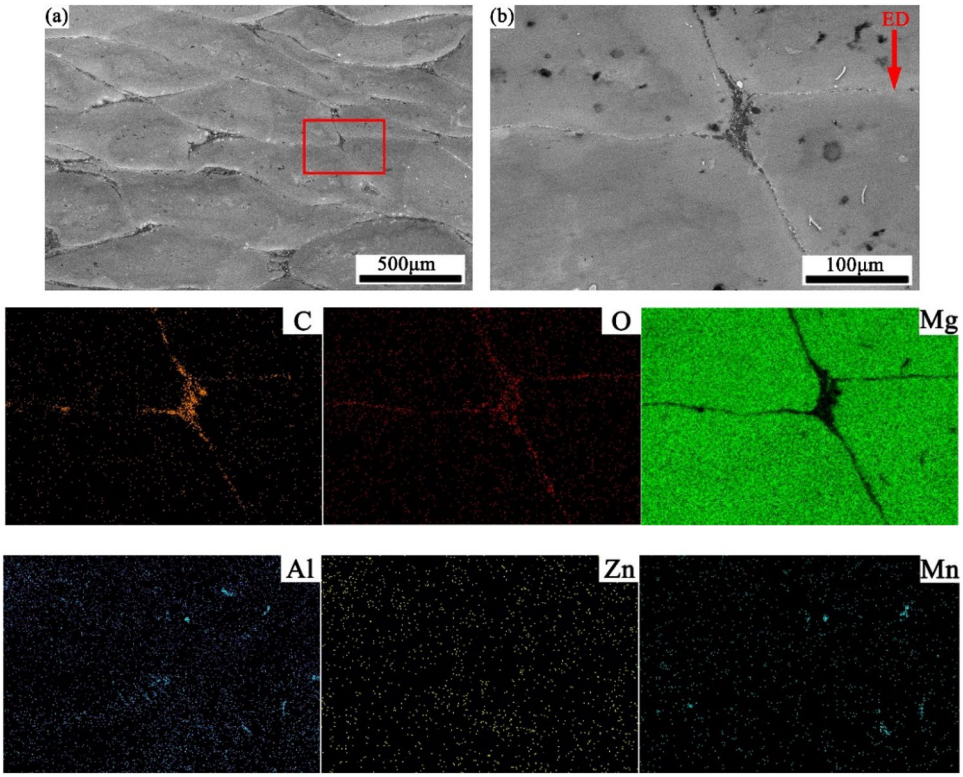

Fig. 1 SEM images of (**a**, **b**) the hot-pressed billets observed on the longitudinal section, with (**b**) giving the area enclosed by the red rectangular in (**a**), and EDS elemental maps for C, O, Mg, Al, Zn, and Mn in the hot-pressed billets

the fragment of SCFs increasing. The average grain sizes of the R8, R11, R25, and R44 composites are 16.0 μm, 13.4 μm, 8.0 μm, and 12.7 μm, respectively (Fig. 2e–h). It should be noted that the average grain size gradually decreases with the increase in extrusion ratio from 8 to 25. However, the grain slightly grows with further increasing the extrusion ratio to 44:1. Previous studies have shown that the average grain size should be strongly related to the extrusion conditions, and the relationship can be described using the Zener–Hollomon (Z) parameter [20]:

$$\Delta\bar{d} = AZ^{-n} \tag{1}$$

$$Z = \dot{\varepsilon}\exp\left(\frac{Q}{RT}\right) \tag{2}$$

where $\bar{d}$ is the average grain size, A is a constant, n is the power law exponent, $\dot{\varepsilon}$ is the extrusion strain rate, Q is the diffusion activation energy, R is the gas constant, and T is the temperature. In the present study, the extrusion speed is fixed at 0.8 mm/s, so the extrusion strain rate $\dot{\varepsilon}$ can be calculated by the following equation [21]:

$$\dot{\varepsilon} = \frac{6D_B^2 V_R \ln ER}{D_B^3 - D_E^3} \tag{3}$$

where D_B is the diameter of the billet, D_E is the diameter of the extrusion bar, V_R is the extrusion speed, and ER is the extrusion ratio. It is expected that with increasing extrusion ratio, the average grain size should decrease according to these equations, while the average grain size of the R44 composite is larger than that of the R25 composite, which may be attributed to deformation heating. Sung et al. [22] reported that the deformation heat is increasing with the strain rate at the deformation zone, leading to the grain size becoming coarse gradually.

Figure 3 shows SEM images of the as-extruded R8 and R25 composites. High-magnification SEM images are obtained from the red rectangles in Fig. 4a and b. Note that the SCFs are more homogeneously distributed within the matrix in R25 composites than that in R8 composites (Fig. 3a and b). Previous studies have analyzed that the higher deformation strain promotes the broken and refinement of second phases, then the refined second phases dispersive distributed along the matrix flowing [17, 23]. Therefore, the SCFs in the as-extruded composites gradually disperse and expand to extended areas within the matrix under a larger extrusion ratio. Furthermore, the high-magnification SEM images indicate that cracks emerge in R8 composites (Fig. 3c), while R25 composites exhibit compact surfaces without any cracks (Fig. 3d). Thus, properly increasing the extrusion ratio is beneficial to improve the bonding degree of the composite and obtain compacted material.

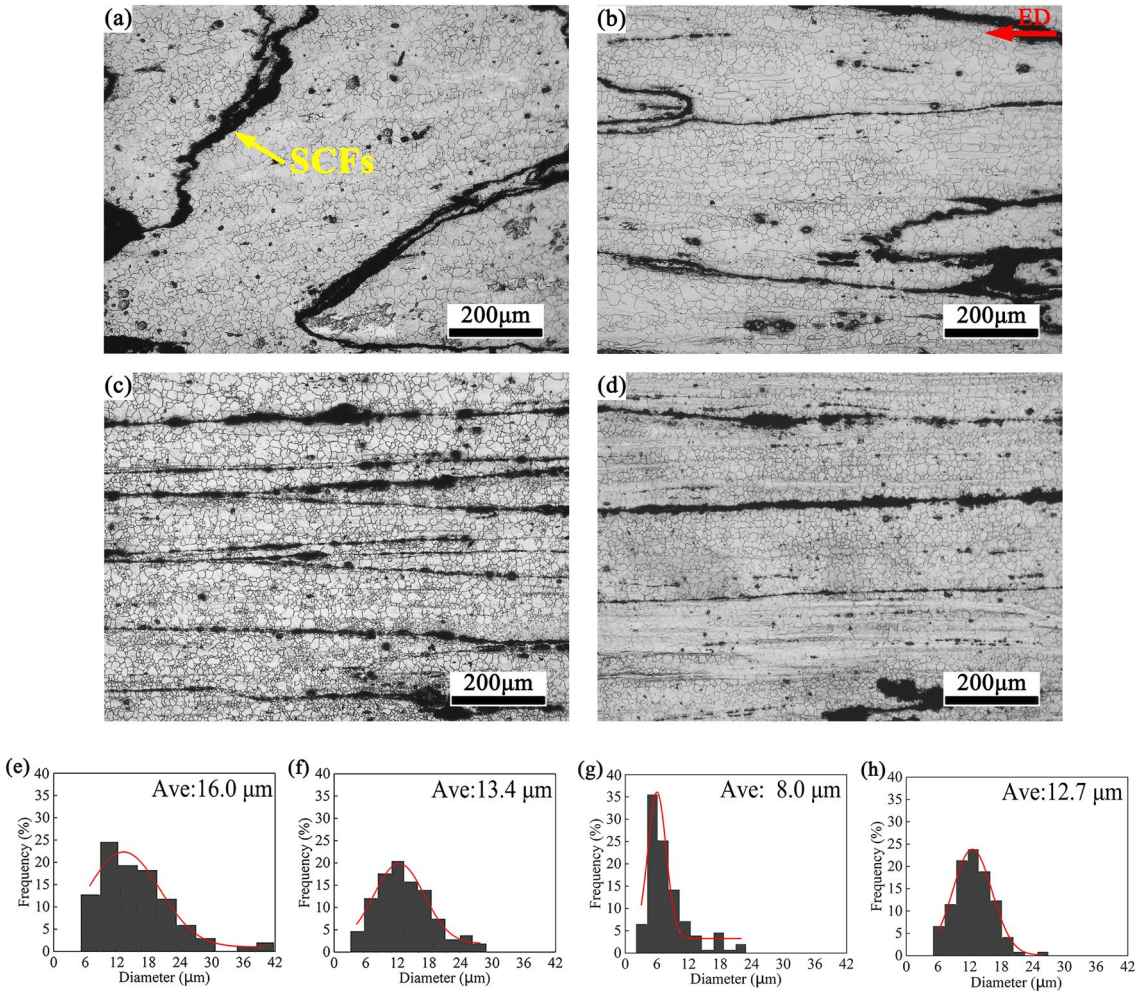

Fig. 2 OM images and grain size distribution of the SCFs/AZ31composites: (**a**, **e**) R8, (**b**, **f**) R11, (**c**, **g**) R25, and (**d**, **h**) R44

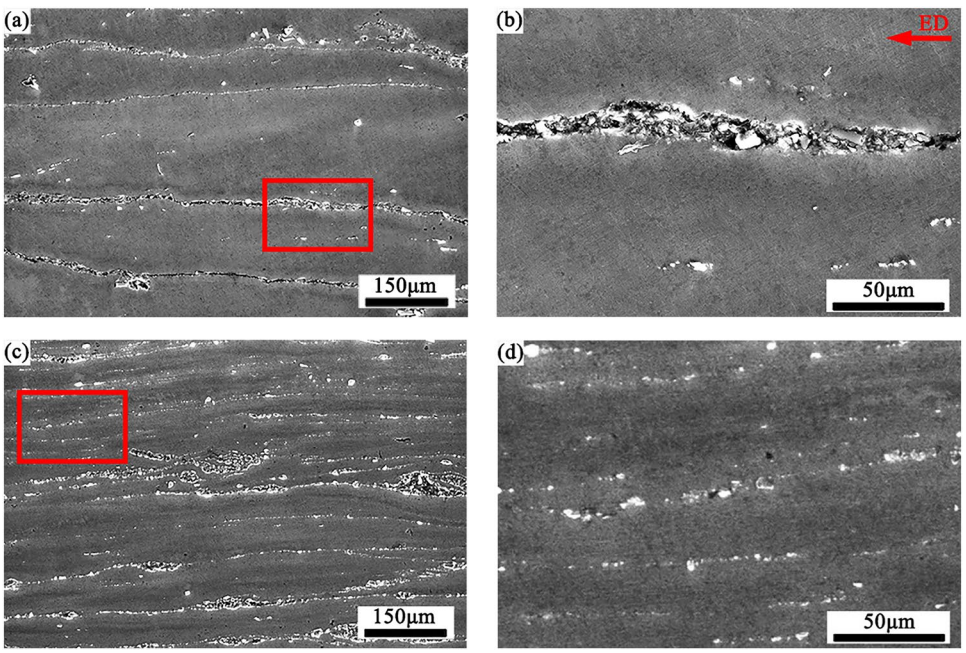

Fig. 3 SEM images of the SCFs/AZ31 composites: (**a**, **b**) R8, (**c**, **d**) R25. (**b**) and (**d**) giving the area enclosed by the red rectangular in (**a**) and (**c**), respectively

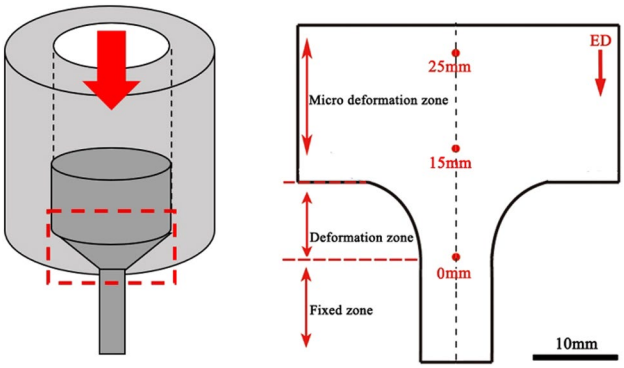

Fig. 4 Schematic drawing of the microstructural observation locations of extrusion specimen during hot extrusion

3.3 Microstructure Evolution During Hot Extrusion

To understand the microstructure evolution of the composite during the hot extrusion process and the influence of SCFs on the recrystallization behavior of α-Mg matrix, the interrupted as-extruded R25 composite is observed at different locations right below the extrusion die by OM and EBSD. According to the deformation degree of the billet, the interrupted composite can be divided into the micro-deformation zone, severe deformation zone, and fixed zone, as shown in Fig. 4. To further reveal the effect of SCFs additions, the AZ31 billet based on chips was fabricated by same process conditions.

Figure 5 shows OM images of the interrupted extrusion composites at 25 mm above the die exit. At the initial stage of deformation, it can be approximately regarded as no deformation in both AZ31 alloy and composites, and the interface of the original AZ31 chips still exists, marked by yellow arrows (Fig. 5a and c). As shown in Fig. 6b and d, the grain sizes of the AZ31 alloy and composites are less than 100 µm. According to Jiang et al. [24], the grain size of as-homogenized AZ31 alloy is significantly larger, 150 µm, which is observed at 15–20 mm below the die exit, suggesting that dynamic recrystallization behavior already occurs in the hot-press process. Moreover, some fine DRXed grains are observed around preexisting second phases and SCFs, marked by the blue rectangle in Fig. 6b and d, indicating the preexisting second phases and SCFs leading to the formation of new grains via particles simulated nucleation (PSN) mechanism [25].

Figure 6 shows the EBSD result of the interrupted extrusion AZ31 sample and composite sample at 15 mm above the die exit. With continuous extrusion, the amount of the fine DRXed grains gradually increase. Some twins exist in the coarse grains of the AZ31 sample and composite sample. In the initial stage of deformation, the twinning-induced DRX mechanism is the dominant deformation mechanism [26]. Meanwhile, many fine DRXed grains are formed at the original grain boundaries (Fig. 6), indicating that the discontinuous DRX (DDRX) mechanism is involved in microstructure evolution [27]. Within the original grains, there are also lots of fine DRXed grains and many low-angle

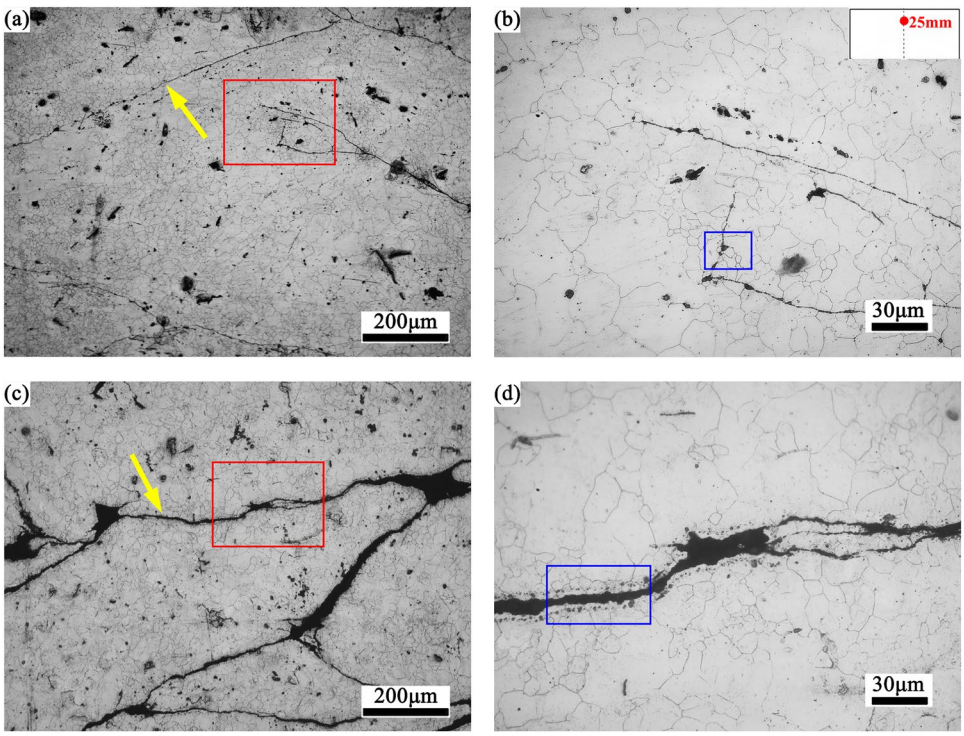

Fig. 5 OM images of the interrupted extrusion sample at 25 mm below the die exit: (**a**, **b**) AZ31, (**c**, **d**) composite. (**b**) and (**d**) giving the area enclosed by the red rectange in (**a**) and (**c**), respectively

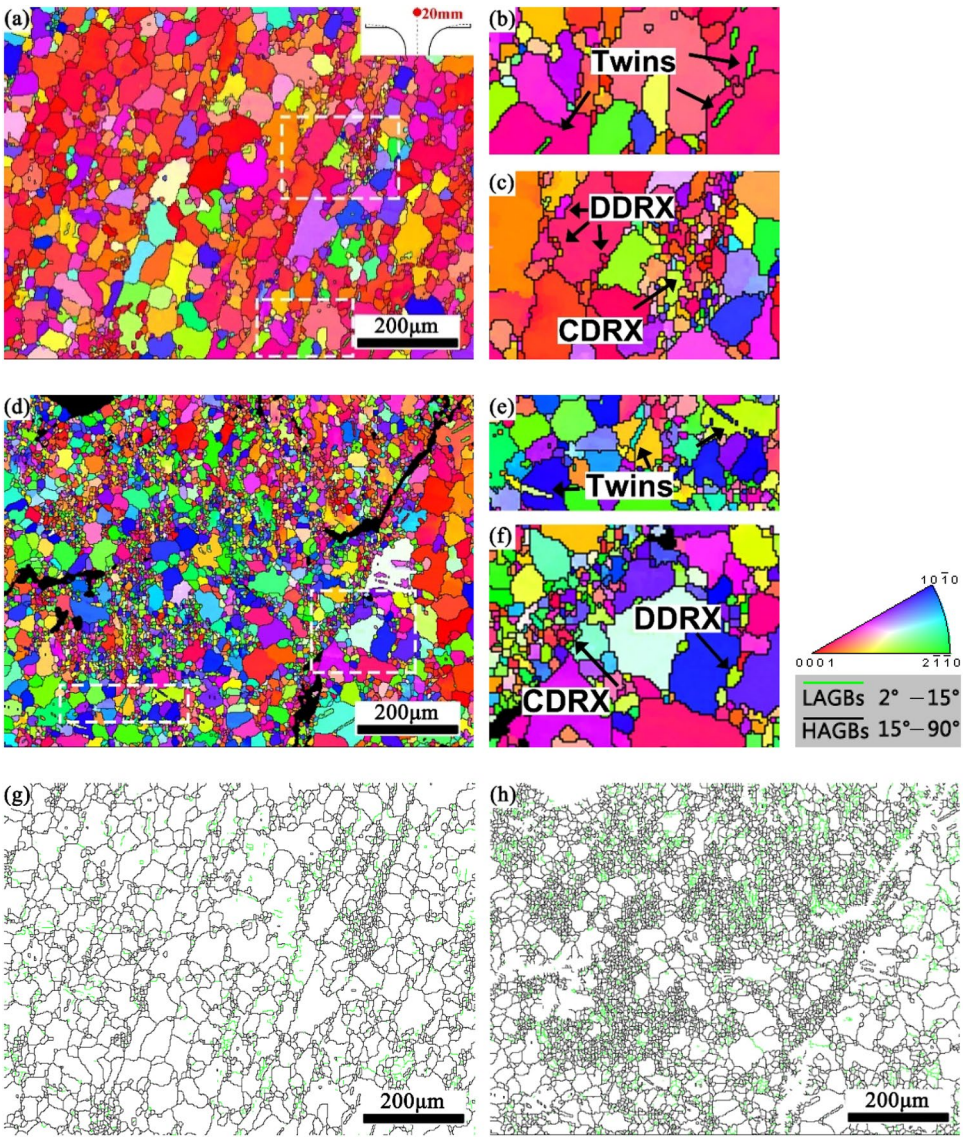

Fig. 6 EBSD results of the interrupted extrusion samples at 15 mm below the die exit: (**a**)–(**f**) inverse pole figure (IPF) maps; (**g**) and (**h**) grain boundary map. (**a**, **b**, **c**, **g**) AZ31 alloy; (**d**, **e**, **f**, **h**) composite

grain boundaries (LAGBs) (green lines), which subdivide the original grains into small sub-grains with similar size to the fine DRXed grains. Usually, during deformation process, a mass of dislocations would activate and accumulate in the vicinity of these LAGBs, then under increasing strain, the LAGBs transform into the fresh DRXed grains with high-angle grain boundaries (HAGBs) via the continuous DRX (CDRX) mechanism [28]. Furthermore, compared with the AZ31 alloy, the DRX behavior of the composite is enhanced, and more fine grains are formed by the CDRX mechanism. Two possible reasons are taken into consideration. Firstly, as strong barriers for the movement of dislocations, SCFs promote the dislocations pile-up and provide favorable sites for the formation of sub-grains, which would contribute to enhancing the nucleation rates of the DRXed grains [29, 30]. Secondly, owing to the large thermal expansion mismatch between α-Mg matrix ($CTE_{\alpha\text{-Mg}} = 25 \times 10^{-6}\ K^{-1}$) and SCFs ($CTE_{SCFs} = 0.5 \times 10^{-6}\ K^{-1}$) [31], a high dislocation density would be generated in the vicinity of the SCFs [32], leading to the transformation of LAGBs to HAGBs and the improvement of the CDRX during hot extrusion. Therefore, twinning, DDRX and CDRX play dominant roles in the hot deformation process, and the SCFs could promote the recrystallization.

3.4 Mechanical Properties of the As-Extruded Samples

Figure 7 shows the mechanical properties of the as-extruded composites at room temperature. The yield strength (YS), ultimate tensile strength (UTS), and elongation of fraction (EL) of as-extruded R8 composites are only 138 MPa, 195 MPa and 3.6%, respectively. Although the SCF is a promising reinforcement for metal, a low extrusion ratio has an unfavorable effect on the combination of composite,

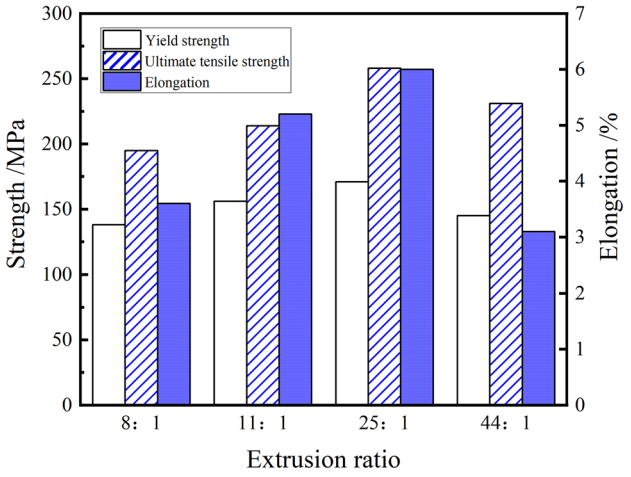

Fig. 7 Tensile properties of the SCFs/AZ31 composite at different extrusion ratios

as shown in Fig. 4b, and then the crack is easily initiating and propagating at the bonding between SCFs and α-Mg matrix when loading along extrusion direction. Therefore, the R8 composite shows poor mechanical properties. The R25 composite exhibits higher YS, UTS, and EL of 171 MPa, 258 MPa, and 6.0%, respectively. The strength enhancement with a higher extrusion ratio can be mainly attributed to the following factors. Firstly, according to the fine-grain strengthening mechanism, the strength is inversely proportional to the grain size of the alloy. The fine grains of R25 composite can effectively improve the strength of composite. Secondly, the mismatch in the coefficient of thermal expansion between α-Mg and SCFs leads to dislocation generation at the interface, which contributes to dislocation strengthening [33]. Thirdly, with higher strain, the SCFs are fractured into abundant small segments and homogeneously distributed within the matrix, which is beneficial to inhibit dislocation movement and improve deformation resistance via dislocation strengthening [13]. However, in the present composite fabricated by solid-state synthesis, the bond between α-Mg matrix and SCFs is mainly mechanical bond, resulting in limited stress transfer. Further study should shed light on improving interface bonding between α-Mg matrix and SCFs to increase the mechanical strength of composites.

Figure 8 shows the fracture morphology of the as-extruded R8, R11, R25, and R44 composites after the tensile test. As presented in the low-magnification fracture morphology of the composites (Fig. 8a–d), with low extrusion ratio (R8 and R11), fracture mainly occurs in the combined surface of AZ31 chips, indicating the poor bonding strength of the composites, which is agreed with the discussion of Fig. 5. With extrusion ratio increasing, the macroscopical fracture surface of composites tends to smooth (Fig. 8c, and d). Additionally, the high-magnification fracture morphology of R25 and R44 composites mainly exhibit ductile dimple fractured features (Fig. 8e and f). There are some deep dimples in the microstructure of the R25 composites, due to its small grain size, which contribute to the higher EL of the R25 composites.

4 Conclusion

In this study, the SCFs/AZ31 composite fabricated by solid-state synthesis with different extrusion ratios was investigated in detail, the dynamic recrystallization mechanisms of the composites were confirmed, and the strengthening mechanisms were analyzed. The conclusions obtained are as follows:

(1) After hot extrusion, full dynamic recrystallization occurs in all the extruded composites. The composite extruded at an extrusion ratio of 25:1 exhibits the finest DRXed grains, which is attributed to the higher extrusion strain rate and homogeneous distribution of SCFs. The dynamically recrystallized grains are mainly formed by PSN, CDRX and DDRX mechanisms. The addition of SCFs not only improves the DRX by promoting recrystallization nucleation, but also accelerates the transformation of LAGBs to HAGBs, then improves CDRX, during hot extrusion.

(2) The composite extruded with an extrusion of 25:1 exhibits the best tensile properties (YS ~ 171 MPa, UTS ~ 258 MPa and EL ~ 6.0%). The high strength can be mainly attributed to the grain refinement strengthening caused by refined DRXed grains and the dislocation strengthening inspired by added SCFs. With the increase in extrusion ratio, the refined grains and the compact combination of the composite are the major causes of the improvement of elongation. These results indicate that the addition of SCFs and the suitable fabrication method are beneficial for obtaining high mechanical performance of magnesium matrix composites.

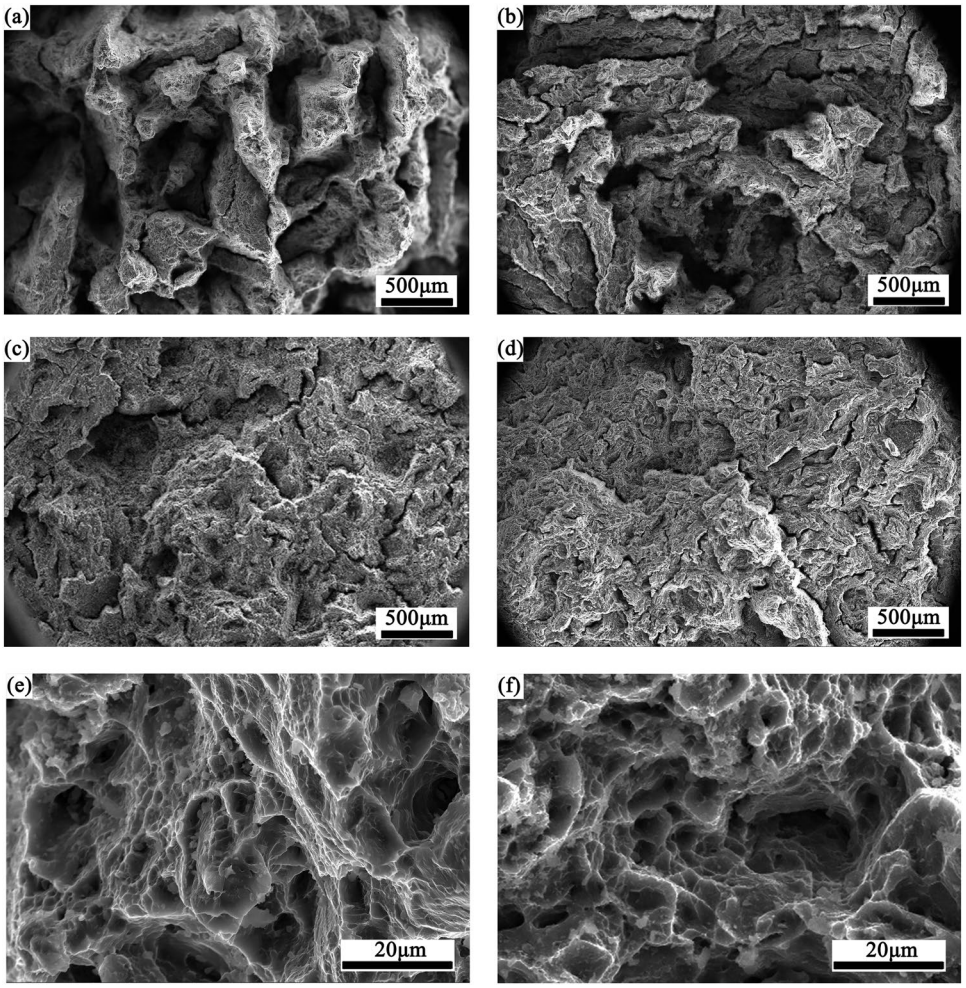

Fig. 8 SEM images of tensile fracture surfaces of the SCFs/AZ31 composites at different extrusion ratios: (**a**) 8:1; (**b**) 11:1; (**c**, **e**) 25:1; (**d**, **f**) 44:1

Acknowledgements This work was supported by the Natural Science Foundation of Heilongjiang Province (LH2020E083), Scientific Research Starting Foundation of Anhui Polytechnic University of China (2020YQQ036), Research Project of Anhui Polytechnic University of China (Xjky2022025), and the Open Research Fund of Anhui Key Laboratory of High-Performance Non-Ferrous Metal Materials (YSJS-2023-06).

References

1. Liu Z Y, Chen B, Zhao P Y, Yu L P, Pei Z R, Zhou B, and Zeng X, *Vacuum* **207** (2023) 111668. https://doi.org/10.1016/j.vacuum.2022.111668
2. Yang Z, Wang G, Chao X, Wang M, Nakata T, Hongyu X, Geng L, and Kamado S, *J Mater Res Technol* **21** (2022) 3756. https://doi.org/10.1016/j.jmrt.2022.11.015
3. Dai Y, Xiao M, Hu Y, Yang Y, Jiang B, Zheng T, Dong L, Yang B, and Zheng C, *J Mater Res Technol* **20** (2022) 1570. https://doi.org/10.1016/j.jmrt.2022.07.166
4. Li W J, Deng K K, Zhang X, Wang C J, Kang J W, Nie K B, and Liang W, Microstructures, tensile properties and work hardening behavior of sicp/Mg-Zn-Ca composites. *J Alloys Compd* **695** (2017) 2215. https://doi.org/10.1016/j.jallcom.2016.11.070
5. Zhang J H, Nie K B, Deng K K, Han J G, and Yi J Y, *Compos Commun* **27** (2021) 100. https://doi.org/10.1016/j.coco.2021.100847
6. Shen M J, Wang X J, Zhang M F, Hu X S, Zheng M Y, and Wu K, *Mater Sci Eng A* **601** (2014) 58. https://doi.org/10.1016/j.msea.2014.02.035
7. Xiong B W, Wang Z J, Wang C W, Xiong Y Z Y, and Cai C, *Intermetallics* **106** (2019) 59. https://doi.org/10.1016/j.intermet.2018.12.010
8. Yang Z, Xu H Y, Wang Y, Hu M L, and Ji Z S, *Mater Res Express* **6** (2019) 106547. https://doi.org/10.1088/2053-1591/ab38d0
9. Xu H Y, Zhao Y, Hu M L, and Ji Z S, *Results Phys* **17** (2020) 103074. https://doi.org/10.1016/j.rinp.2020.103074
10. Ye J, Chen X, Luo H, Zhao J, Li J, Tan J, Yang H, Feng B, Zheng K, and Pan F, *J Magn Alloys* **10** (2022) 2266. https://doi.org/10.1016/j.jma.2022.06.012
11. Sun S, Deng N, Zhang H, He L, Zhou H, Han B, Gao K, and Wang X, *J Mater Res Technol* **15** (2021) 1789. https://doi.org/10.1016/j.jmrt.2021.09.015
12. Feng J, Song K X, Liang S H, Guo X H, and Li S L, *J Mater Res Technol* **20** (2022) 1470. https://doi.org/10.1016/j.jmrt.2022.07.131
13. Yuan Q H, Zhou G H, Liao L, Liu Y, and Luo L, *Carbon* **127** (2018) 177. https://doi.org/10.1016/j.carbon.2017.10.090
14. Nie K B, Guo Y C, Deng K K, and Kang X K, *J Alloys Compd* **792** (2019) 267. https://doi.org/10.1016/j.jallcom.2019.04.028

15. Xiao L, Yang G Y, Chen J M, Luo S F, Li J H, and Jie W Q, *Mater Sci Eng A* **744** (2019) 277. https://doi.org/10.1016/j.msea.2018.11.142
16. Nie K B, Zhu Z H, Deng K K, and Han J G, *J Magn Alloy* **8** (2020) 676. https://doi.org/10.1016/j.jma.2020.04.006
17. Yan K, Sun J P, Liu H, Cheng H H, Bai J, and Huang X, *Mater Lett* **242** (2019) 87. https://doi.org/10.1016/j.matlet.2019.01.089
18. Asgharzadeh H, Joo S H, and Kim H S, *Metall Mater Trans A* **45** (2014) 4129. https://doi.org/10.1007/s11661-014-2354-6
19. Nakata T, Xu C, Ajima R, Matsumoto Y, Shimizu K, Sasaki T T, Hono K, and Kamado S, *Mater Sci Eng A* **712** (2018) 12. https://doi.org/10.1016/j.msea.2017.11.085
20. Xu C, Nakata T, Qiao X G, Jiang H S, Sun W T, Chi Y C, Zheng M Y, and Kamado S, *Mater Sci Eng: A* **685** (2017) 159. https://doi.org/10.1016/j.msea.2016.12.121
21. Yang Z, Xu C, Nakata T, and Kamado S, *Mater Sci Eng A* **800** (2021) 140330. https://doi.org/10.1016/j.msea.2020.140330
22. Park S H, You B S, Mishra R K, and Sachdev A K, *Mater Sci Eng A* **598** (2014) 396. https://doi.org/10.1016/j.msea.2014.01.051
23. Liu H, Ju J, Yang X, Yan J, Song D, Jiang J, and Ma A, *J Alloys Compd* **704** (2017) 509. https://doi.org/10.1016/j.jallcom.2017.02.107
24. Jiang M G, Xu C, Yan H, Fan G H, Nakata T, Lao C S, Chen R S, Kamado S, Han E H, and Lu B H, *Acta Materialia* **157** (2018) 53. https://doi.org/10.1016/j.actamat.2018.07.014
25. Yu Z J, Xu C, Meng J, Liu K, and Fu J L, *Mater Sci Eng A* **762** (2019) 138080. https://doi.org/10.1016/j.msea.2021.142521
26. Chi Y Q, Xu C, Qiao X G, and Zheng M Y, *J Alloys Compd* **789** (2019) 416. https://doi.org/10.1016/j.jallcom.2019.03.066
27. Liu W, Su Y, Zhang Y, Chen L, Hou H, and Zhao Y, *J Magn Alloys* **11** (4), (2023) 1408. https://doi.org/10.1016/j.jma.2022.03.018
28. Jiang M G, Xu C, Yan H, Lu S H, Nakata T, Lao C S, Chen R S, Kamado S, and Han E H, *Sci Rep* **8** (1), (2018) 16800. https://doi.org/10.1038/s41598-018-35170-4
29. Zhang L, Wang Q, Liao W, Guo W, Li W, Jiang H, and Ding W, *Mater Sci Eng A* **689** (2017) 427. https://doi.org/10.1016/j.msea.2017.02.076
30. Pan H, Qin G, Huang Y, Ren Y, Sha X, Han X, Liu Z Q, Li C, Wu X, Chen H, and He C, *Acta Materialia* **149** (2018) 350. https://doi.org/10.1016/j.actamat.2018.03.002
31. Yang Z, Xu H Y, Wang Y, Hu M L, and Ji Z S, *Results Phys* **12** (2019) 888. https://doi.org/10.1016/j.rinp.2018.12.039
32. Chen F Y, Ying J M, Wang Y F, Du S Y, Liu Z, and Huang Q, *Carbon* **96** (2016) 836. https://doi.org/10.1016/j.carbon.2015.10.023
33. Rashad M, Pan F S, Hu H H, Asif M, Hussain S, and She J, *Mater Sci Eng A* **630** (2015) 36–44. https://doi.org/10.1016/j.msea.2015.02.002